Bioactive Materials 38 (2024) 195–206

Contents lists available at ScienceDirect

Bioactive Materials

journal homepage: www.keaipublishing.com/en/journals/bioactive-materials

3D-printed, citrate-based bioresorbable vascular scaffolds for coronary artery angioplasty

Yonghui Ding [a,b], Liam Warlick [c], Mian Chen [b], Eden Taddese [c], Caralyn Collins [a,d], Rao Fu [a,d], Chongwen Duan [a,b], Xinlong Wang [a,b], Henry Ware [a,d], Cheng Sun [a,d,*], Guillermo Ameer [a,b,e,**]

[a] Centre for Advanced Regenerative Engineering (CARE), Northwestern University, Evanston, IL 60208, USA
[b] Department of Biomedical Engineering, Northwestern University, Evanston, IL 60208, USA
[c] Department of Materials Science and Engineering, Northwestern University, Evanston, IL 60208, USA
[d] Department of Mechanical Engineering, Northwestern University, Evanston, IL 60208, USA
[e] Department of Surgery, Feinberg School of Medicine, Northwestern University, Chicago, IL 60611, USA

A B S T R A C T

Fully bioresorbable vascular scaffolds (BVSs) aim to overcome the limitations of metallic drug-eluting stents (DESs). However, polymer-based BVSs, such as Abbott's Absorb, the only US FDA-approved BVS, have had limited use due to increased strut thickness (157 μm for Absorb), exacerbated tissue inflammation, and increased risk of major cardiac events leading to inferior clinical performance when compared to metallic DESs. Herein we report the development of a drug-eluting BVS (DE-BVS) through the innovative use of a photopolymerizable, citrate-based biomaterial and a high-precision additive manufacturing process. BVS with a clinically relevant strut thickness of 62 μm can be produced in a high-throughput manner, i.e. one BVS per minute, and controlled release of the anti-restenosis drug everolimus can be achieved by engineering the structure of polymer coatings to fabricate drug-eluting BVS. We achieved the successful deployment of BVSs and DE-BVSs in swine coronary arteries using a custom-built balloon catheter and BVS delivery system and confirmed BVS safety and efficacy regarding maintenance of vessel patency for 28 days, observing an inflammation profile for BVS and DE-BVS that was comparable to the commercial XIENCE™ DES (Abbott Vascular).

1. Introduction

Atherosclerotic coronary artery disease (CAD) is responsible for significant morbidity, mortality, and healthcare costs worldwide. Endovascular therapies, such as the implantation of vascular stents after angioplasty, have become the mainstream treatment for CAD. The original vascular stents, bare-metal stents, were simple mechanical scaffolds which prevented vessel collapse after angioplasty; however, they are associated with high restenosis rates (20–60 %) [1,2]. Drug-eluting stents (DESs) loaded with anti-stenosis drugs, such as sirolimus and everolimus, effectively reduced the restenosis rate to < 5 % [3]. However, the permanent presence of a metallic scaffold in the blood vessel causes a range of side effects, including impaired vasomotion, compromised adaptive arterial remodeling, and long-term foreign-body responses [4–6]. Additionally, when permanent stents fail, the revision surgery to revascularize tissue is complicated and can be associated with dismal outcomes [7,8]. The challenges associated with permanent metal stents have prompted the development of bioresorbable vascular scaffolds (BVSs). Metal-based BVSs, typically made of magnesium or iron-based alloys, have not been clinically adopted due to their rapid resorption or detrimental corrosion products, which leads to frequent post-surgical restenosis [9]. Polymer-based BVSs have emerged as a promising solution for providing initial support to prevent blood vessel recoil while slowly degrading to eliminate residual foreign materials and eventually restoring blood vessel functions such as vasomotion [10]. However, current polymer-based BVSs, such as Absorb GT1 (Abbott Vascular, Santa Clara, CA), the only U.S. Food and Drug Association (FDA)-approved BVS, are associated with a high incidence of late thrombosis (3.5 % vs 0.9 % at 2 years) and major adverse cardiac events (11 % vs 7.9 % at 2 years). These BVSs also require prolonged dual-antiplatelet therapy to prevent clotting when compared to metal DESs [11,12]. Probable causes of these issues include: 1) the oxidative stress and exacerbated tissue inflammation induced by the degradation product of poly (l-lactic acid) (PLLA); and 2) the increased strut thickness (157 μm) compared to a metallic DES (61–80 μm in strut thickness) leading to larger disturbance of local blood flow. The thickness of these

Peer review under responsibility of KeAi Communications Co., Ltd.
* Corresponding author. Centre for Advanced Regenerative Engineering (CARE), Northwestern University, Evanston, IL, 60208, USA.
** Corresponding author. Centre for Advanced Regenerative Engineering (CARE), Northwestern University, Evanston, IL, 60208, USA.
E-mail addresses: c-sun@northwestern.edu (C. Sun), g-ameer@northwestern.edu (G. Ameer).

https://doi.org/10.1016/j.bioactmat.2024.04.030
Received 17 February 2024; Received in revised form 25 April 2024; Accepted 27 April 2024

struts also limits the number of patients that can be treated with these devices.

We tackle the aforementioned challenges via the implementation of a two-fold strategy. To address the inflammatory responses to PLLA, we investigate the use of citrate-based polymers, such as polydiolcitrates, to fabricate BVSs. Polydiolcitrates have demonstrated intrinsic antioxidant properties that reduce chronic inflammatory responses associated with PLLA [13]. Of note, polydiolcitrates have been recently used for the fabrication of FDA-cleared biodegradable implantable medical devices currently used in musculoskeletal surgeries [14,15]. Furthermore, we and others have shown that polydiolcitrates have intrinsic thromboresistant properties and support the formation of a functional endothelium [16–18]. To address the adverse impact of increased strut thickness, we refined the high-precision additive manufacturing process flow to fabricate drug-eluting BVSs (DE-BVSs) with a clinically relevant strut thickness of less than 100 μm.

The fundamental understanding of material properties and manufacturing as they relate to *in vivo* performance and clinical feasibility of a BVS is critical. In this work, to maximize clinical translation, we first improved our manufacturing efficiency, resulting in the simultaneous fabrication of at least 8 BVSs with a strut thickness of 65 μm and a length of 10 mm within 7 min, i.e. one scaffold per minute. To ensure these scaffolds are capable of delivering anti-restenosis drugs, on par with current DESs on the market, we developed a biodegradable citrate-based polymer coating that can be sprayed onto the 3D-printed BVSs to achieve programmable drug loading and controlled release rates. This polymer/drug coating method can be applied to any tissue regeneration porous scaffold to achieve controlled drug release. Additionally, to allow for the successful deployment of the BVSs, we have developed a customized balloon catheter assembly. Finally, we demonstrate the successful *in vivo* deployment, safety, and performance of BVSs and DE-BVSs in swine coronary arteries. At 28 days, both BVSs and DE-BVSs demonstrated performance equivalent to a clinically used cobalt chromium (CoCr) DES, the XIENCE Pro DES from Abbott Vascular. Therefore, we show that: 1) citrate-based BVSs can be safe and effective; and 2) additive manufacturing of DE-BVSs with strut dimensions comparable to those of metal DES is feasible.

2. Results

2.1. MicroCLIP allows high-throughput printing of BVS with reduced strut dimensions

The poly (1,12-dodecanediol citrate) (PDC) and poly (1,8-octanediol citrate) (POC) pre-polymer was prepared by the condensation reaction between citric acid and 1,12-dodecanediol or 1,8-octanediol, respectively. The analysis of PDC and POC by mass spectrometry indicated the presence of various molecular structures with different combinations between diol and citrate acid (Fig. S1). For example, the PDC spectra consisted of the combination of 1,12-dodecanediol and two citrate acids (*m/z* 573.3), while the repeating unit is the combination of one 1,12-dodecanediol and one citrate acid (*m/z* 358). The POC spectra consisted of the combination of two 1,8-dodecanediol peaks and one citrate acid (*m/z* 471) as the base structure, followed by the addition of one citrate acid (*m/z* 645) and the addition of one 1,8-dodecanediol (*m/z* 773). The photopolymerizable PDC and POC were prepared by incorporating methacrylate groups into the PDC or POC pre-polymer. The presence of the C=C bonds in the methacrylate PDC (mPDC) and methacrylate POC (mPOC) were validated by ^{1}H Nuclear Magnetic Resonance (NMR) (Fig. S1). The 3D-printable ink was formulated by mixing mPDC pre-polymer (75 wt%) with a photo initiator Irgacure 819, a co-initiator EDAB, and ethanol as a solvent. The additive manufacturing technology utilized in this study, referred to as microscale continuous liquid interface production (MicroCLIP) (Fig. 1A), offers uniformity of the projected UV light intensity with a pixel size of 4.0 μm. These features allow for high-throughput simultaneous fabrication of 8 BVSs per print with lengths of 10 mm within a time frame of 7 min (one stent per minute) (Fig. 1B) and also enable the high fabrication fidelity of BVSs with struts as thin as 62 μm (Fig. 1C).

The key properties of 3D-printed BVSs, including degradation, antioxidative properties, and biocompatibility, were characterized. The mass loss and the reduction in the radial strength were observed following accelerated degradation in 0.1 mM sodium hydroxide (Fig. 1D). The 3D printed BVSs retained the intrinsic antioxidant properties of PDC [13], as shown by their strong capability to scavenge free radicals (Fig. 1E). In contrast, limited free radical scavenging was

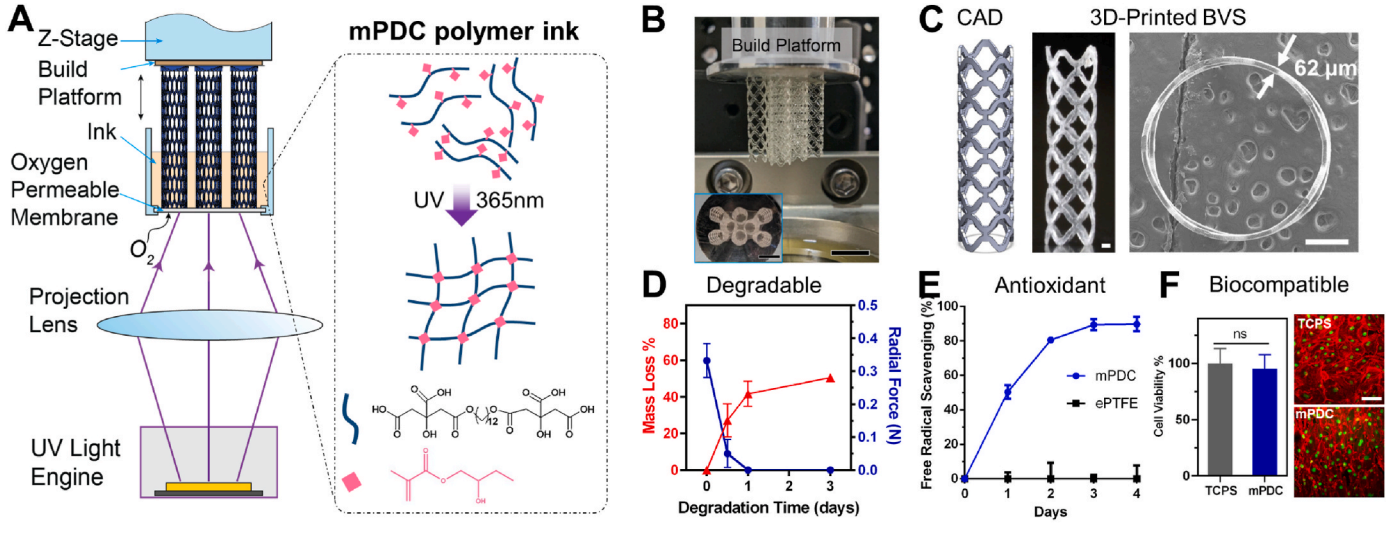

Fig. 1. Fabrication and characterization of the citrate-based, 3D-printed bioresorbable vascular scaffold (BVS). (A) Schematic of microscale continuous liquid interface production (MicroCLIP) process for the fabrication of BVS using mPDC polymer ink. (B) Digital optical image of 8 BVSs that were simultaneously 3D-printed. (C) BVS CAD model and 3D-printed BVS with 62 ± 3 μm strut thickness (left: optical image; right: top view SEM image) Scale bars: 500 μm. (D–F) 3D-printed, citrate polymer-based BVS has biodegradable, antioxidant, and biocompatible properties. (D) BVS accelerated degradation in 0.1 mM NaOH showing mass loss (%) and radial force at 30 % compression over time (n = 6). (E) BVS and ePTFE (reference material) free radical scavenging as per the DPPH assay (n = 3). (F) Viability (MTT assay) and cell morphology (red: F-actin, green: nuclei) of HUVECs that were grown on TCPS and mPDC. ns: no significance. n = 3. Scale bar: 20 μm.

associated with medical grade expanded polytetrafluoroethylene (ePTFE), a commonly used material for vascular grafts and stent grafts. The biocompatibility with vascular endothelial cells was validated by the high viability and healthy cell morphology when cells were grown on the 3D-printed mPDC, which were comparable to the cells grown on the tissue culture polystyrene (TCPS) (Fig. 1F).

2.2. mPOC coating of BVS enables controlled release of everolimus

DESs consisting of a metal stent with a thin polymer coating as the carrier of anti-stenosis drugs have been developed to combat intimal hyperplasia. Current approaches to control the release of a drug from a stent have challenges that impact endothelial tissue recovery. Here, we applied mPOC as the drug-carrying polymer coating for 3D-printed BVSs and show that the controlled release of everolimus is achieved (Fig. 2). Drug-eluting BVSs (DE-BVSs) were fabricated by sequentially depositing a polymer-drug layer (mPOC with everolimus) and a barrier layer (mPOC only) with an ultrasonic sprayer (Fig. 2A). A conformal and uniform coating with a smooth surface finish was obtained on both luminal and abluminal surfaces of the DE-BVSs, as shown by scanning electron microscopy (SEM) images (Supporting InformationFig. S2). The strut thickness was increased from 62 ± 3 μm for the bare BVS to 99 ± 4 μm for the DE-BVS (drug layer and barrier layer). The successful incorporation of everolimus within the coating was confirmed by ATR-FTIR analysis (Supporting Information Fig. S3). The characteristic peaks for pure everolimus, including 1643 cm^{-1} (C=O), 1451 cm^{-1} (C–H), and 990 cm^{-1} (C–H) [19], were detected in the spectra of DE-BVS (drug and drug + barrier), but they were not visible in the spectra of BVS with pure polymer coating not containing the drug.

Under normal physiological conditions, a set of release profiles were achieved with DE-BVSs by programming the order of the coatings (drug *versus* drug + barrier) and the loading concentrations of drug (Fig. 2B). For example, a burst release was observed for the DE-BVS with drug layer only, e.g. DE-BVS_1 wt% Drug, with 92 % of everolimus being released within 7 days. A more sustained release was achieved for the DE-BVS with drug + barrier coatings, e.g. DE-BVS_1 wt% Drug + Barrier, with only 60 % and 80 % of everolimus being released within 7 and 14 days, respectively. Furthermore, the total amount of everolimus released from the DE-BVS could be augmented by increasing the loading concentration of everolimus from 1, 1.5, 2, to 4 wt%. It was found that the loading concentration of 1.5 wt% everolimus yielded a similar total amount of everolimus release within 84 days compared to the commercial XIENCE DES. Therefore, the loading concentration of 1.5 wt% was selected for subsequent *in vitro* and *in vivo* evaluation. Notably, the DE-BVS_1.5 wt% Drug + Barrier device in this study achieved a more controlled release profile than the commercial XIENCE DES.

Following drug release in PBS with 10 % ethanol (pH 7.4, 37 °C) for 84 days, the degradation of DE-BVSs was assessed by measuring the changes of their radial forces and mass. It was found that the radial force per 8 mm long BVS dropped by 20–45 % within 84 days (Fig. 2C), accompanied by a mass loss of 4.6–6.5 % (Fig. 2D). The differences in radial forces between BVSs (Ctrl) and DE-BVSs (Drug and Drug + Barrier) were found to be statistically insignificant both before ($p > 0.808$) and after ($p > 0.116$) 84 days of degradation. Although there seemed to be a lower mean mass loss for the DE-BVS with drug coating compared to others, no significant difference was observed ($p > 0.397$). This indicates that the inclusion of thin coating layers of biodegradable polymer neither enhances the radial strength nor alters the degradation behavior when compared to uncoated BVSs. The limited mechanical reinforcement is likely attributed to the less densely crosslinked thin polymer coatings, created exclusively through UV curing, in contrast to the base polymer struts, which underwent both UV and thermal curing. The exclusion of thermal curing for the coating polymer aims to prevent thermal damage to the loaded everolimus.

2.3. DE-BVS inhibits proliferation of smooth muscle cells (SMCs) with limited impact on endothelial cells (ECs)

The polymer coating of current DES and the released everolimus interact with surrounding vascular tissues by inhibiting the proliferation of SMCs to reduce the restenosis rates while delaying the recovery of ECs and subsequent vascular healing [20]. Vascular cell responses were

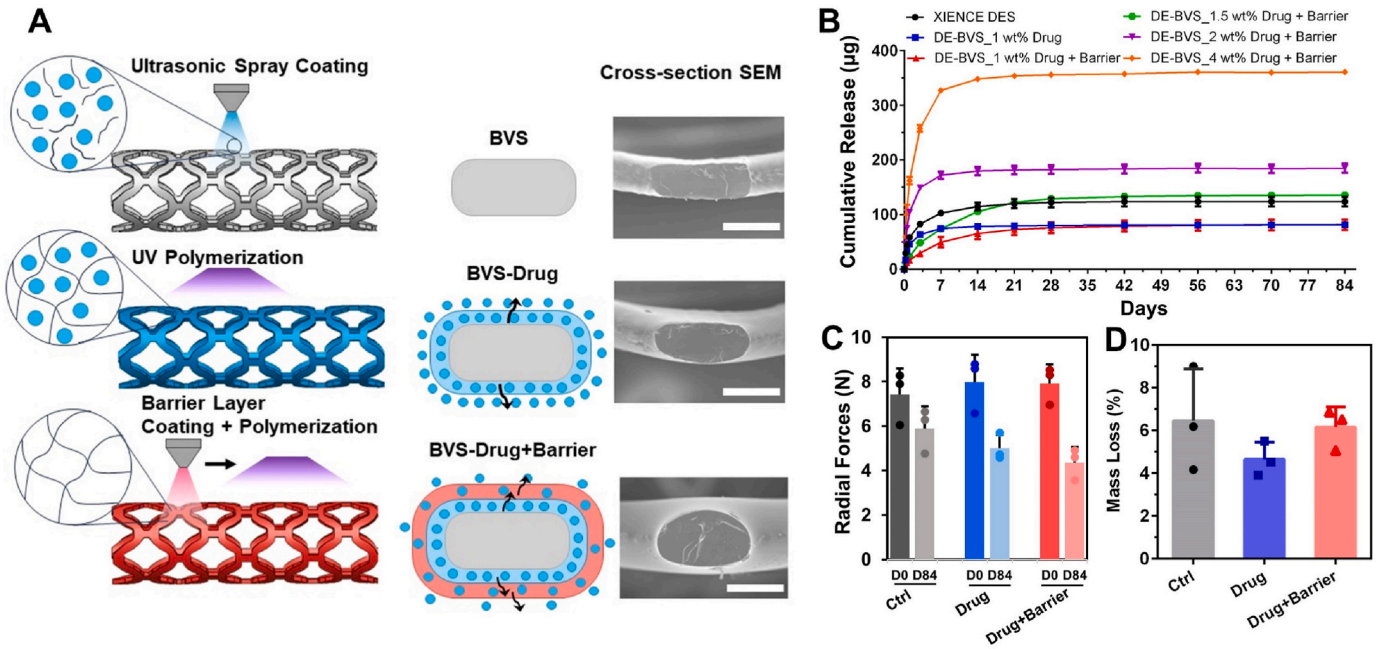

Fig. 2. Fabrication of drug eluting BVS (DE-BVS) with strut thickness under 100 μm and programmable drug eluting profiles. (A) Schematic and scanning electron microscopy (SEM) images of cross-sectional views showing radial strut thickness of bare BVS (62 ± 3 μm) and DE-BVS with drug coating only (77 ± 4 μm), and DE-BVS with coatings of drug + barrier (99 ± 4 μm). Scale bar: 100 μm. (B) Various drug eluting profiles for 84 days were achieved by manipulating coating structure and drug loading concentrations (1, 1.5, 2, and 4 wt%) (n = 4, $p > 0.05$). (C, D) Degradation properties including (C) radial forces at 50 % compression at day 0 (D0) and day 84 (D84) as well as (D) the mass loss of DE-BVS in the PBS at 37 °C for 84 days (n = 3, $p > 0.05$).

evaluated by seeding and growing human umbilical vein endothelial cells (HUVECs) and human aortic smooth muscle cells (HAoSMCs) on 3D-printed mPDC substrates with three types of coatings: 1) mPOC polymer without drug (Ctrl), 2) mPOC polymer coating with 1.5 wt% everolimus (Drug), and 3) mPOC polymer coating with 1.5 % everolimus plus a mPOC barrier layer (Drug+Barrier) (Fig. 3). High cell viability and healthy cell morphologies of HAoSMCs and HUVECs were observed on the control substrate, confirming cytocompatibility of mPOC polymer as a coating for vascular scaffolds. The released everolimus from the polymer/drug coating prominently inhibited the proliferation and viability of both HAoSMCs and HUVECs. Interestingly, the coatings of drug + barrier significantly inhibited SMC viability and spreading with limited impact on EC viability and morphology. These *in vitro* results demonstrate the importance of controlled release of everolimus from DE-BVSs in modulating cell responses.

2.4. A customized balloon catheter system enables the in vivo deployment of BVSs

To prepare for the *in vivo* evaluation of scaffolds, we investigated the possibility of deploying our 3D-printed BVSs and DE-BVSs using standard procedures in current interventional cardiology clinical practice. We first optimized the scaffold geometry and conditions of 3D printing and post-processing to ensure the mechanical competence of the scaffolds. As a result, 3D-printed scaffolds could withstand cycling mechanical loading, including radial compression and expansion between the original diameter of 3.0 mm and final, crimped diameter of 1.1 mm, without strut fracture (Fig. 4A and B and Supporting InformationFig. S4). Interestingly, we observed spontaneous self-expansion and an increase of scaffold diameter following the scaffold compression onto the balloon catheter (Supporting InformationFig. S4). This self-expansion can potentially lead to the dislodgement of the compressed scaffold from the balloon during the advancement of the balloon catheter toward the targeted location inside the artery. In addition, balloon-expanding stents are often favored over self-expanding stents for percutaneous coronary intervention due to their ability to provide more precise control over dimensions, simpler deployment process, and higher radial forces compared to self-expanding stents in current clinical practice [21].

To ensure the successful deployment of BVSs and maintain clinical relevance, a customized balloon catheter system was developed. A modification of a commercial balloon angioplasty catheter was achieved by introducing two components: a locking sheath and a stopper (Fig. 4C). The locking sheath, fabricated with medical-grade expanded poly (tetrafluoroethylene), was used to keep the compressed scaffold in place (Fig. 4C–ii). The locked scaffold within the sheath was assembled on the balloon catheter with a stopper at the far end of the balloon (Fig. 4C–iii). During the deployment process (Fig. 4C–i), the assembled device was first advanced into the targeted location inside the artery (Step 1 or S1). While retracting the sheath, the scaffold was first moved along with the sheath until it was stopped by the stopper, which was made by a thin tube of medical grade polyetheretherketone (S2), leading to the release of the scaffold from the locking sheath (S3). The scaffold was then expanded against the surrounding vessel wall following the inflation (S4) of the balloon. Finally, following the deflation (S5) of the balloon, the entire customized balloon catheter system was retracted and withdrawn from the body (S6).

Using this customized balloon catheter system and procedure, 3D-printed scaffolds, including 8 BVSs and 8 DE-BVSs were successfully deployed into coronary arteries of 8 domestic healthy swine (Fig. 4D). As a basis for clinical relevance, 8 commercial everolimus-eluting DES (Abbott's XIENCE™ Pro S) (standard of care reference devices), were also deployed into coronary arteries of the swine via their preassembled catheter systems. Each swine received three implants (randomized combinations of BVS, DE-BVS and XIENCE stent) into in three main coronary arteries, including left anterior descending coronary artery (LAD), left circumflex artery (LCX), and right coronary artery (RCA). The angiography images revealed the successful targeting (device expansion and deployment) of the LAD and LCX (Fig. 4D i-ii). Although the BVS was not visible under fluoroscopic imaging due to the intrinsic radiolucency of the polymer, BVS struts showed strong contrast under intravascular ultrasound (IVUS) (Fig. 4D–iii), allowing us to track the

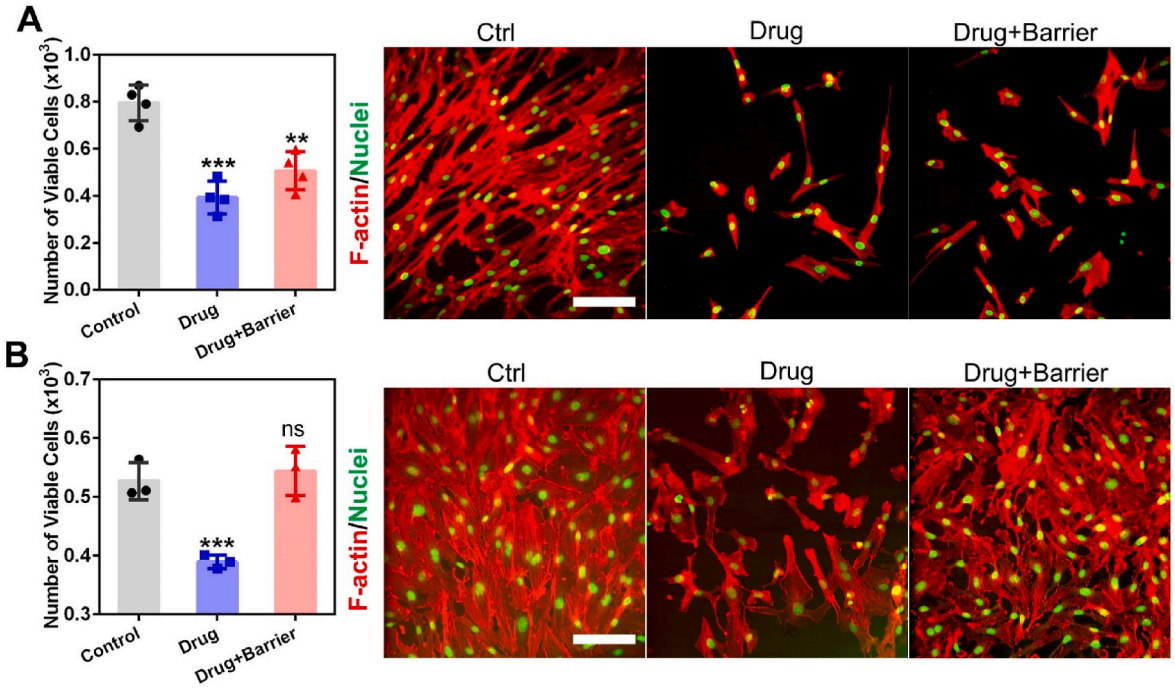

Fig. 3. *In vitro* responses of (A) human aortic smooth muscle cells (HAoSMCs) and human umbilical vein endothelial cells (HUVECs) to DE-BVSs. Cell viability was evaluated by Alamar Blue Assay (n = 3 or 4; $^{**}p < 0.01$ and $^{***}p < 0.001$ vs. control). Cell morphologies were observed by confocal microscope following the immunostaining of F-actin and nuclei. Scale bars: 200 μm.

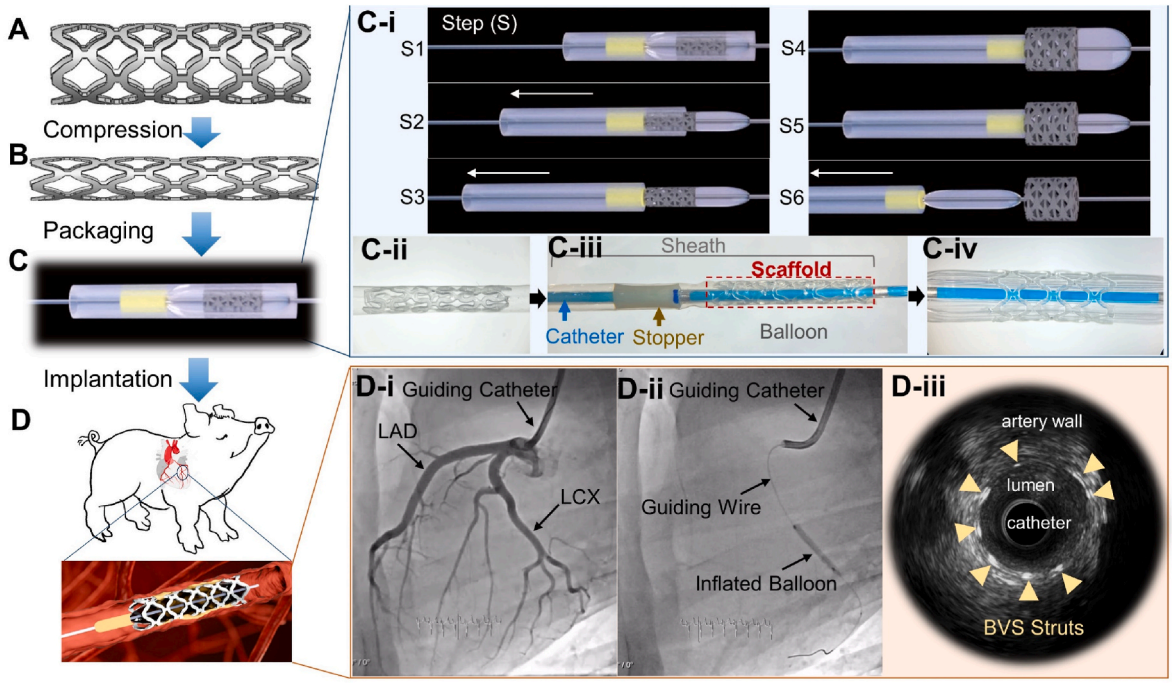

Fig. 4. The custom-built BVS delivery system enables the *in vivo* deployment of BVS in swine coronary arteries. The fabricated scaffolds (A) were compressed (B), assembled onto the custom-built delivery system (C), and implanted into swine coronary arteries (D). (C-i) The schematic illustration of scaffold deployment steps, including step 1 (S1), the assembled scaffold on the balloon catheter; S2, the retraction of the sheath with the scaffold kept in place by the stopper; S3, the release of the scaffold from the sheath; S4, the inflation of the balloon along with the expansion of the scaffold; S5, the deflation of the balloon; and S6, the retraction of the balloon catheter. (C-ii) Digital optical image of the compressed scaffold locked inside the catheter sheath. (C-iii) Digital optical image of the scaffold assembled onto the custom-built delivery system. (C-iv) Digital optical image of the expanded scaffold on the balloon catheter. (D-i) X-ray images from angiography show the left anterior descending coronary artery (LAD) and left circumflex artery (LCX) of a swine. (D-ii) X-ray image shows the inflated balloon to expand the scaffold in the LCX. (D-iii) The intravascular ultrasound (IVUS) image of the scaffold struts (as indicated by arrows) within the coronary artery following implantation.

scaffold *in vivo*. There were no complications such as acute thrombosis, dissection, malposition, or collapse during the procedures identified by immediate angiography and IVUS.

2.5. BVSs and DE-BVSs demonstrate comparable efficacy and safety to commercial XIENCE DES in swine coronary arteries

All animals remained healthy throughout the 28-day duration of the study. None of the coronary arteries with scaffolds or stents showed evidence of luminal thrombosis on day 28 post-implantation. There was no evidence of myocardial infarction, epicardial hemorrhage, or other obvious abnormalities along the coronary arteries according to gross examination of the heart.

Both BVSs and DE-BVSs induced similar levels of arterial narrowing to that induced by XIENCE DES as measured by IVUS over 28 days (Fig. 5A). The Movat's pentachrome and hematoxylin and eosin (H&E) stained tissue sections showed that: 1) the lumen remained patent without any evidence of thrombosis; and 2) all scaffold/stent struts were fully covered by neointima tissue with well-organized structures (Fig. 5B). Quantitative analyses showed that there were no statistically significant differences in luminal area, neointimal area, neointimal thickness, and area stenosis when comparing the BVS or DE-BVS with the XIENCE DES (Fig. 5C and Supporting InformationTable S1). The mean values of neointimal area and area restenosis induced by the XIENCE DES were lower than those induced by BVS and DE-BVS, which was mainly ascribed to the significant arterial remodeling response to the implantation in 2 out of 8 swine. The neointima area of DE-BVS and XIENCE DES groups were 4.6 ± 4.4 and 2.6 ± 1.2 mm^2, respectively, which were not significantly different from that of the BVS group, i.e. 3.8 ± 2.2 mm^2 and $p > 0.46$. Similarly, there was no statistically significant difference in the area restenosis among these three groups, i.e. BVS (62.0 ± 23.8 %), DE-BVS (61.8 ± 17.5 %), and XIENCE DES (48.6 ± 22.1 %); $p > 0.49$. These results suggest that vascular responses to BVS and DE-BVS observed in this study are largely comparable to those of the commercial XIENCE DES for all key measures at 28 days post-implantation. Interestingly, the bare polymer BVS displayed comparable levels of restenosis to the DE-BVS.

2.6. BVSs and DE-BVSs do not induce significant inflammatory responses relative to commercial XIENCE DES

The inflammatory response plays an important role in the healing of the injured arteries and the development of in-stent restenosis. Inflammation was acute and present only in stented arterial sections. As macrophages are one of the major inflammatory cells that infiltrate into stented arterial walls, we performed immunostaining for CD86, a marker of macrophages with a pro-inflammatory (or M1) phenotype, and CD163, a marker of macrophages with a pro-healing (or M2) phenotype (Fig. 6A). It was found that the infiltrated macrophages were predominantly present in the peri-strut region. The $CD86^+$ and $CD163^+$ macrophages largely overlapped with each other, which is in line with the high complexity of macrophage phenotypes [22]. The quantification of the area covered by the $CD86^+$ or $CD163^+$ macrophages and ratio of $CD163^+/CD86^+$ show that there was no significant difference in the number of macrophages and their phenotypes among the three groups, i.e. BVS, DE-BVS, and XIENCE DES (Fig. 6B), which was consistent with the quantified inflammation score from the histopathology analyses.

2.7. BVSs and DE-BVSs support the regeneration of smooth muscle and endothelium

To better understand the healing process, we studied the influence of scaffolds/stents on the growth of smooth muscle tissue and re-coverage

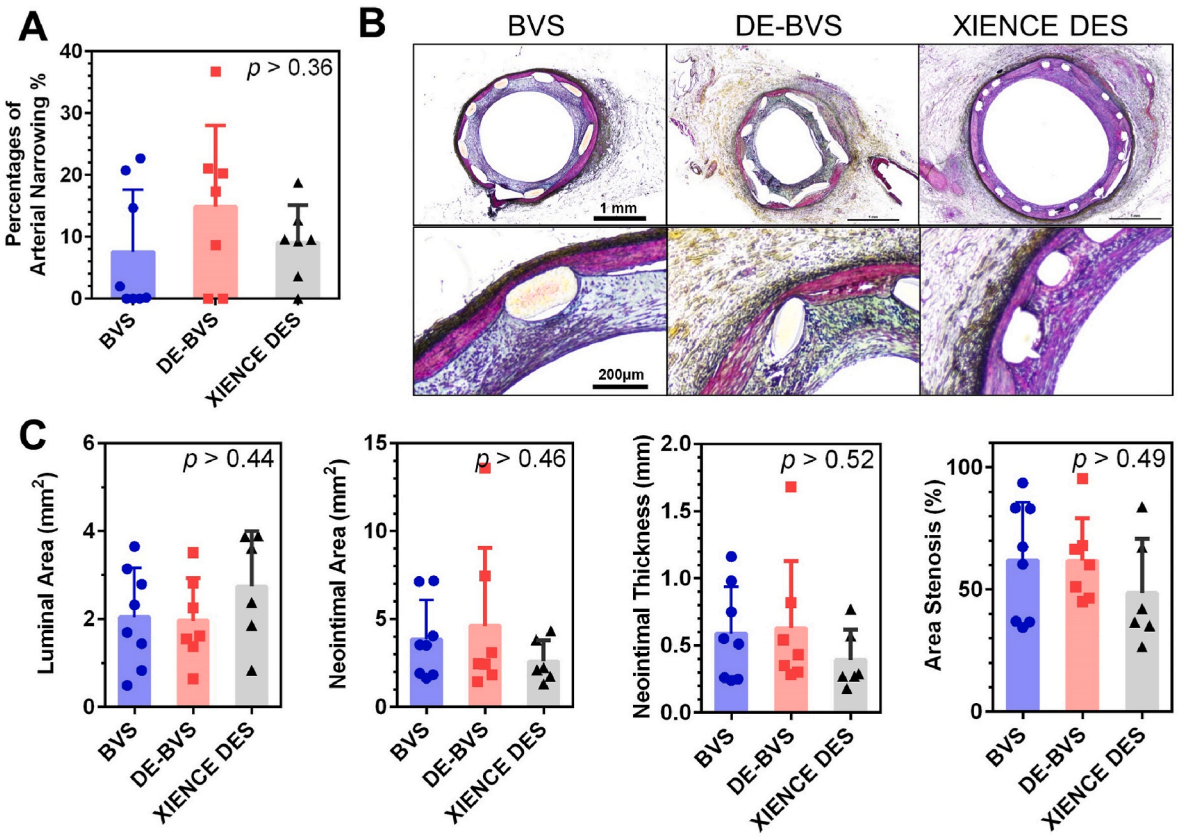

Fig. 5. BVSs and DE-BVSs are safe and effective in keeping the arteries patent after implantation for 28 days in swine coronary arteries. (A) Quantification of the arterial narrowing over 28 days as measured via intravascular ultrasound within three stents, i.e. BVS, drug-eluting BVS (DE-BVS), and XIENCE DES. (B) Movat pentachrome stains of swine coronary arteries with scaffolds/stents. (C) Quantification of neointimal thickness, neointimal area, medial area, neointimal stenosis, and inflammation scores of stented arteries via the histomorphometry analysis of tissue sections.. (n = 8 for BVS; n = 7 for DE-BVS; n = 6 for XIENCE DES.)

of endothelium in swine coronary arteries. As shown in Fig. 7A, the expression of α-SMA was uniform and smooth muscle cells with spindle shapes were densely packed in the neointima of all scaffolds/stents. The regenerated smooth muscle tissues demonstrated similar shapes and organizational behavior to those in the native media layer. Similar levels of smooth muscle coverage were observed among arteries with BVS, DE-BVS, and XIENCE DES (Fig. 7B). VE-cadherin was used to stain functional endothelial cells. Of note, a thin layer of VE-cadherin^{+} endothelial cells (or endothelium) was observed on the inner most layer of the neointimal tissues for all three groups of scaffolds/stents (as indicated by the white arrow heads on Fig. 7A). Interestingly, BVSs induced a slightly higher percentage of endothelium coverage (72.4 ± 10.0 % for BVS) than the DE-BVS (60.8 ± 10.0 %), although there was no statistically significant difference ($p = 0.18$). These results suggest that the bare BVS may promote favorable formation of a healthy neointimal layer.

3. Discussion

BVSs have been developed with the aim of overcoming the limitations of permanent metallic DESs, which prevent normal vasomotion, hamper further treatment options in stented segments, and can provoke long-term foreign-body responses [11]. Although multiple scaffolds have been or are in development, the clinical use of these scaffolds, such as the only U.S. FDA-approved Absorb BVS (Abbot Vascular), has not gained enough momentum. An example is the withdrawal of the Absorb BVS from the market in 2017. The inferior clinical performance of current BVSs mainly stems from the intrinsic properties of materials used for their fabrication, such as PLLA. The unfavorable material properties include suboptimal mechanical properties, requiring larger strut profiles than metallic stents, and the generation of acidic degradation products, leading to a prolonged inflammatory response. In addition, current scaffold/stent fabrication technologies, such as laser machining, lack the capability of producing patient-specific scaffolds. In this study, we leveraged a citrate-based polymer and a unique 3D printing technology to produce BVSs with biocompatibility, degradation, antioxidative, and drug-eluting properties. Our 3D printing technology offers a highly efficient and tailored production of BVSs [23]. The produced BVSs featuring low profile (sub-100 μm strut thickness and width) and high mechanical strength were evaluated in the coronary arteries of swine and demonstrated comparable *in vivo* performance to the commercially available XIENCE DES (Abbot Vascular) at 28 days post-implantation.

Scaffold designs, particularly regarding strut thickness, can significantly impact clinical outcomes post-implantation. Studies on animal models have demonstrated that thick struts (>100 μm) can increase thrombus formation and impede endothelial recovery compared to thin struts (<100 μm) [24–26]. The majority of polymer BVSs developed to date, such as Absorb, DESolve, Fortitude, and Magmaris, have thick struts exceeding 150 μm in thickness, potentially leading to inferior outcomes compared to thin-strutted metal stents like XIENCE DES (81 μm) [11,26]. In this study, we have produced BVSs with strut thickness of 62 ± 3 μm and DE-BVSs with a combined strut thickness (base + coating layer) of 99 ± 4 μm. In addition, our thin-strutted BVSs exhibit higher radial strength (7.4 ± 1.2 N per device) than the Absorb BVS (2.1 ± 0.03 N) and DESolve BVS (2.8 ± 0.02 N), as reported in a previous study [26,27]. Though the test parameters may vary slightly, these findings suggest that the mechanical strength of the thin-strut BVSs developed in our study is comparable to or even superior to other polymer BVSs. Furthermore, *in vivo* evaluation confirms that our BVSs possess sufficient radial strength to withstand vessel pressure in swine

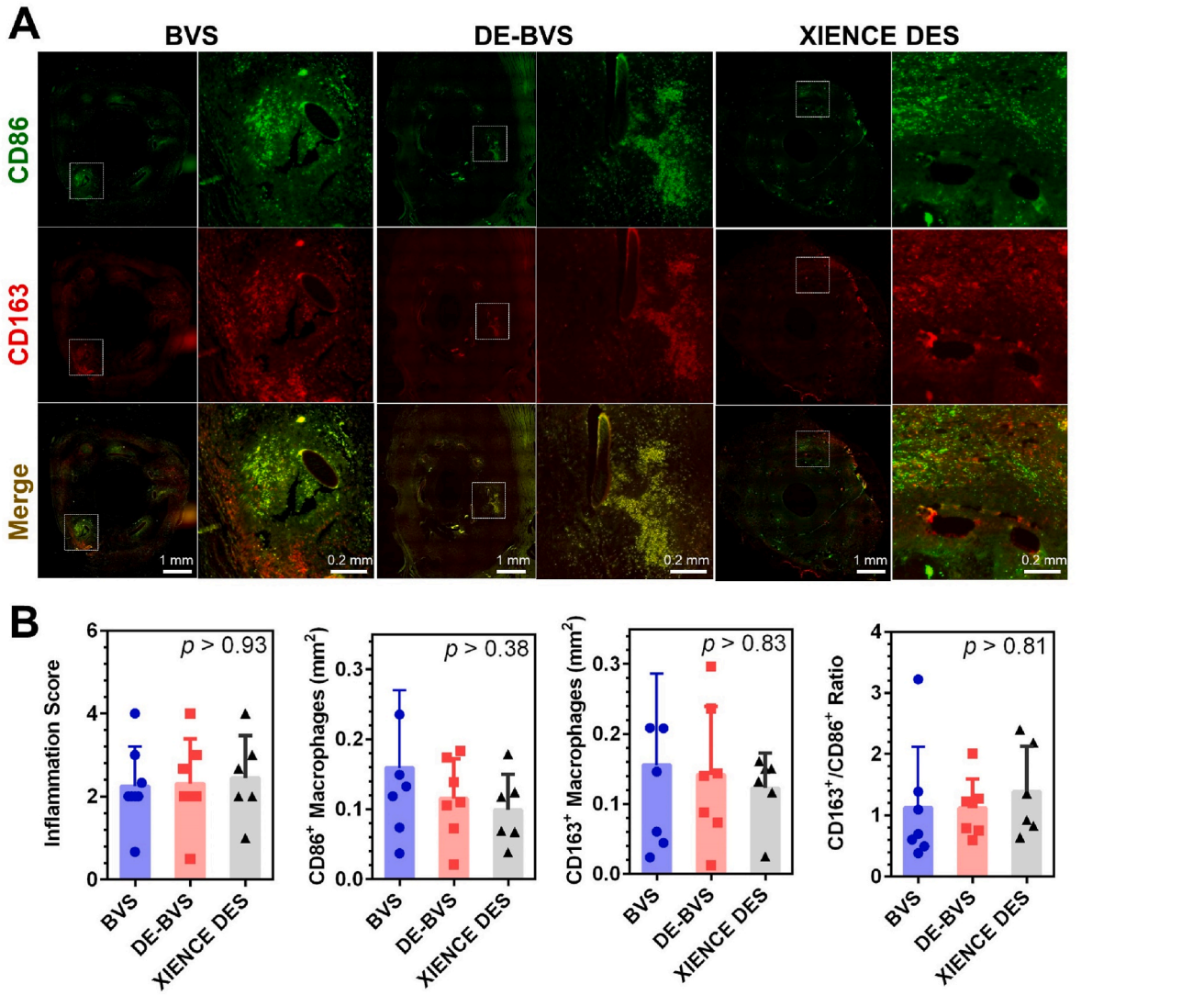

Fig. 6. BVSs and DE-BVSs do not induce significant inflammatory responses relative to commercial XIENCE DESs. (A) Representative fluorescence images of CD86 and CD163-stained artery sections show the presence of macrophages at peri-strut regions. (B) Quantification of inflammation score (from the H&E−stained artery sections as shown in the supporting information Figure S5), the area coverage of $CD86^+$ and $CD163^+$-stained macrophages, and the ratio between $CD86^+$ and $CD163^+$-stained macrophages.

coronary arteries.

The release of anti-restenosis drugs, including parameters such as total amount of drug and drug release rate, plays a critical role in scaffold/stent performance. Achieving the optimal drug release profile to prevent the over-proliferation of smooth muscle tissue without retarding the endothelial recovery remains a challenge. The polymers used to entrap drugs as coatings influence the drug release profile and vascular responses [20,28–31]. Permanent polymers used in the first generation of DES often exhibited late in-stent thrombosis and delayed recovery of endothelium [31]. Polymer coatings can cause chronic inflammatory and hypersensitivity reactions due to the bulk generation of acidic degradation products [20]. In this study, for the first time, we report the use of a biodegradable citrate-based polymer as both a vascular scaffold and a stent coating. Coatings may consist of the polymer and drug (mPOC/everolimus layer) with or whithout a second barrier coating of the polymer alone (mPOC). The addition of the barrier layer results in a more precise and controlled release of everolimus from the device. Moreover, the degradation products from both the mPDC BVSs and the mPOC-coated mPDC BVSs did not trigger significant inflammatory responses at 28 days post-stenting. These findings suggest that mPOC can serve as a promising coating material for drug-eluting scaffolds/stents, offering ample biocompatibility and programmable drug release profiles. In addition, the dosage of the everolimus is another factor to balance the inhibition on SMC and adverse effects on endothelial recovery. In this study, a 1.5 wt% loading concentration of everolimus was chosen in order to match the total amount of everolimus released from the XIENCE DES (Fig. 2B). Despite the pronounced inhibitory effects of released everolimus on smooth muscle cells (SMCs) observed *in vitro* (Fig. 3), these effects appear to diminish *in vivo*, as evidenced by similar SMC coverage between BVS and DE-BVS groups (Fig. 7B). This disparity may stem from the notable phenotypic plasticity exhibited by SMCs. Extensive evidence indicates that SMCs undergo phenotypic alterations when cultured on tissue culture polystyrene [32,33], or within diseased arteries during the progression of atherosclerosis [34,35], in contrast to SMCs from healthy arteries. Variations in SMC phenotypes could lead to different responses to everolimus. Therefore, DE-BVSs might exhibit a more favorable response, such as reduced levels of stenosis, compared to BVSs in the swine model of atherosclerosis. In addition, the release profiles of everolimus could be very different between *in vitro* and *in vivo* settings. In the future, measurements of everolimus concentration in arterial tissue and in blood by pharmacokinetic evaluation are needed for a better understanding of the relationship between drug release and

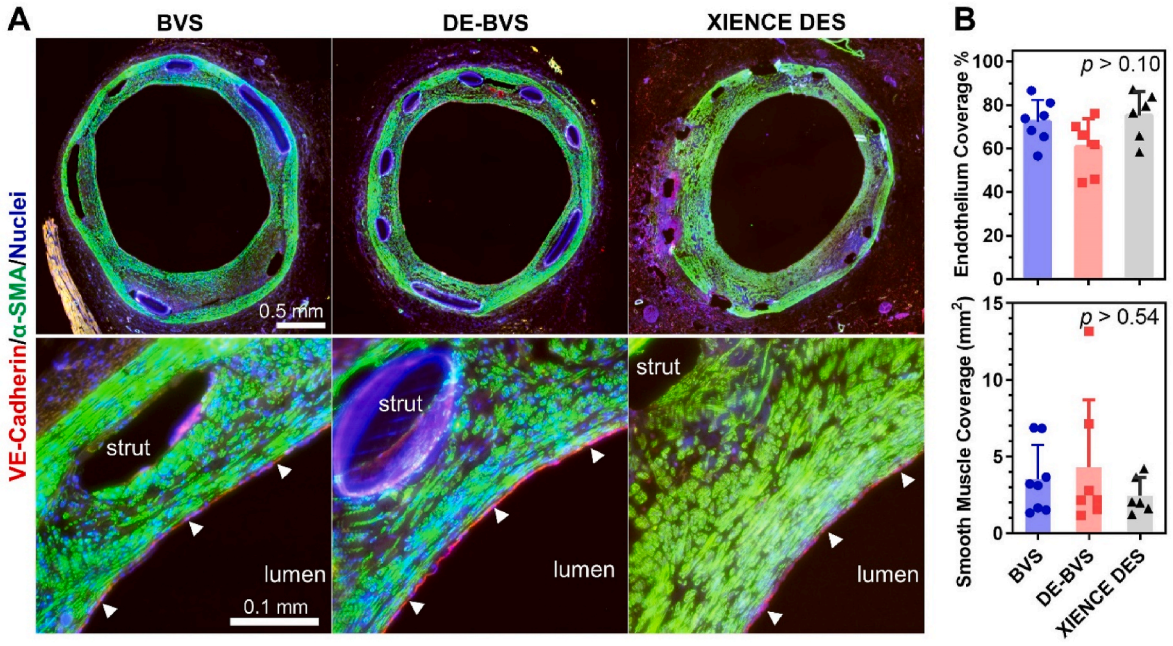

Fig. 7. BVSs and DE-BVSs induce the regeneration of smooth muscle and endothelium. (A) Representative immunofluorescence images of scaffolded/stented arteries probed for VE-cadherin (red, marker of endothelial cells), α-SMA (green, marker of smooth muscle cells), and cell nuclei (blue). The bottom images show enlarged views of selected regions from the top images. The regenerated endothelium (the inner most layer of the arterial wall) is highlighted by the white arrowheads. (B) Quantification of endothelium coverage in scaffolded/stented arteries by measuring and calculating the percentage of region with positive staining of VE-cadherin over the perimeter of lumen. Quantification of smooth muscle coverage in scaffolded/stented arteries by measuring the area of region with positive staining of α-SMA within the neointima.

vascular tissue response.

Delayed and poor strut coverage by neointimal tissue has been recognized as the primary cause for late and very late stent thrombosis following the stent placement [4]. This study showed that all BVSs, DE-BVSs, and XIENCE DESs were completely covered by neointimal tissue without evidence of thrombosis on day 28 post-implantation. Moreover, there were no significant differences in luminal area, neointimal thickness, and area stenosis among the BVS, DE-BVS and XIENCE DES devices, as confirmed by ultrasound imaging examination and histomorphometric analyses. Previous studies showed that the Absorb BVS induced greater levels of neointimal thickness and stenosis than XIENCE DES in the swine coronary artery at 1 month, e.g. 27.9 % stenosis for Absorb vs. 13.5 % stenosis of XIENCE DES with $p = 0.02$ [36]. Similarly, the Arterial Remodeling Technologies (ART) BVS showed a greater level of stenosis than that of a bare metal stent (25.3 % versus 13.2 %) in the healthy swine coronary artery at 1 month [37]. These findings suggest potentially improved vascular healing induced by our BVS.

Vascular inflammation plays critical roles in scaffolding/stenting outcomes since greater inflammation has been correlated with greater neointimal growth and restenosis [38,39]. Previous studies have shown that the mild inflammation induced by Absorb BVS was comparable to that induced by XIENCE DES at 1 month in swine [36]. However, the inflammation for the Absorb BVS became greater than XIENCE DES from 6 to 36 months, which might be ascribed to the acidic degradation product of Absorb BVS [36]. Similarly, the inflammatory scores of the ART BVS in swine increased from 1 to 6 months in swine, which were higher than those of a bare metal stent [37]. In our study, the inflammation scores based on the histomorphometric analyses were largely comparable between BVS, DE-BVS and XIENCE DES. These results were consistent with the similar number of $CD86^+$ (M1 phenotype marker) and $CD163^+$ (M2 phenotype marker) macrophages observed for all scaffolds/stents. M1 macrophages enhance the secretion of pro-inflammatory factors and SMC migration, while M2 macrophages encourage endothelial recovery [40,41].

Endothelium regeneration is an important process for vascular healing [42–45]. In this study, immunohistochemical assessments show that 70–80 % coverage of endothelium occurs on day 28 post-implantation for almost all scaffolded/stented arteries. Previous studies have shown poor endothelium recovery with the Absorb BVS relative to metallic DES in a rabbit model [24]. Despite the significant efforts made to facilitate endothelium adhesion, proliferation, and migration through a variety of strategies [43,44], the mechanism of endothelium regeneration on vascular scaffolds/stent remains unclear [42,46]. A recent study found that blood-circulating monocytes adhere to the luminal surfaces of an acellular vascular graft, differentiate into a mixed endothelial ($CD144^+$) and macrophage ($CD163^+$) phenotype, and further developed into mature endothelial cells *in vitro* and in an ovine model [47]. Interestingly, we had similar findings regarding regenerated endothelium in the scaffolded/stented arteries as 3 out of 8 swine co-expressed the endothelial-specific marker $CD144^+$ (or VE-Cadherin) and the macrophage-specific makers $CD163^+/CD86^+$ (Supporting InformationFig. S6). The regenerated endothelium of the 5 out of 8 swine only expressed $CD144^+$.

In summary, we have designed, fabricated, and tested a biocompatible and regenerative BVS that releases anti-restenosis everolimus in a clinically relevant time frame and dosage. We harnessed a high-resolution and high-speed additive manufacturing process to both produce multiple BVS in parallel, drastically reducing fabrication time for this device, and to reliably print low-profile BVSs with strut thicknesses as small as 62 μm. In doing so, we were able to develop a promising solution for the clinically relevant production of patient-specific scaffolds. By utilizing mPOC coatings as both drug carrier and barrier layers, a controlled release profile of everolimus can be achieved with 3D-printed scaffolds. Beyond showing favorable biocompatibility and intrinsic anti-oxidant properties, these scaffolds were deployed successfully in swine coronary arteries with the use of a custom-built deployment system and process. These scaffolds demonstrated safety and efficacy to maintain vessel patency for 28 days after implantation. Moreover, the BVSs and DE-BVSs tested here favored vascular healing

processes by promoting rapid strut coverage by neointimal tissues and endothelium recovery while limiting the degree of stenosis. Overall, the BVSs and DE-BVSs developed here demonstrate largely comparable preclinical performance in swine coronary arteries as the commercial XIENCE DES, which is the most widely used coronary stent in clinic.

This study also has some limitations. First, the animal evaluation is relatively short. However, the clinically comparable performance of BVSs over 28 days instills confidence for long-term assessments, which is crucial for exploring potential benefits of BVSs like restoring normal vasomotion and mitigating long-term foreign-body responses associated with permanent metal stents. Second, the healthy swine model does not reflect the complexities of coronary intervention in diseased model of atherosclerosis. In the future, a long-term follow-up ($\geq$6 months) and evaluation in atheromatous animal models will be performed to gain more translational perspectives. For instance, the change of lumen area following the partial or full resorption of the scaffold could be an important characteristic to track and distinguish it from metallic stents. Third, the current devices do not have X-ray visibility. Although intravascular imaging techniques like ultrasound and optical coherence tomography offer strong contrast for monitoring devices post-implantation, real-time tracking during deployment is essential. Effective tracking helps to prevent malpositioning and ensures proper expansion. Additionally, it enables the longitudinal assessment of structural changes and degradation behaviors. To address this issue, we are in the process of developing a BVS equipped with biodegradable radiopaque markers positioned at both ends of the scaffold for real-time tracking under fluoroscopy in our upcoming animal study. Furthermore, we have recently incorporated the widely employed clinical contrast agent, iodixanol (Visipaque™, GE Healthcare), into the struts of polymer scaffolds [48]. This innovation facilitates tracking of the device using micro-computed tomography (micro-CT) for a minimum of 4 weeks. Nevertheless, the ongoing challenge lies in balancing X-ray visibility with the mechanical flexibility of the device, posing a hurdle for its application in vascular scaffolds. Lastly, *in vivo* evaluations of pharmacokinetics and citrate-based polymer degradation are needed to gain better insights into: 1) the drug release profiles in the arterial tissues and blood flow; and 2) the resorption characteristics of scaffolds and the impact on their mechanical function and vascular healing.

4. Materials and methods

4.1. Materials and devices

All chemicals were obtained from Millipore Sigma unless otherwise noted. Everolimus was purchased from Selleckchem. The control device, XIENCE™ Pro S everolimus-eluting DES was obtained from Abbott Vascular.

4.2. mPDC and mPOC synthesis and characterization

Methacrylate poly(1,12-dodecamethylene citrate) (mPDC) and Methacrylate poly(1,8-octanediol

citrate) (mPOC) was synthesized by following our previously reported protocol [17]. Briefly, citric acid and 1,12-dodecanediol at molar ratio of 2:3 or citric acid and 1,8-octanediol at molar ratio of 1:1 were melted (165 °C, 22 min), co-polymerized (140 °C, 60 min), purified, and freeze-dried to yield PDC of POC pre-polymer. Every 22 g PDC or POC pre-polymer was dissolved in tetrahydrofuran (180 mL) with imidazole (816 mg) and glycidyl methacrylate (17.8 mL), reacted (60 °C, 6 h), purified, and freeze-dried to yield mPDC or mPOC pre-polymer.

The characterization of PDC and POC pre-polymer was performed by a Bruker AmaZon SL Mass Spectrometer equipped with an Electrospray Ionization source (ESI) and an Ion Trap Mass Analyzer. The sample analysis was done with direct loop injection, using ethanol as the carrier solvent/mobile phase. The acquisition method was set up to perform an Alternate Positive and Negative ion acquisition, collecting both positive and negative ion information. The characterization of mPDC or mPOC pre-polymer was performed by proton nuclear magnetic resonance (^{1}H NMR) using deuterated dimethyl sulfoxide (DMSO-d_6) as the carrier solvent.

4.3. Fabrication of BVS

To formulate mPDC ink for 3D printing of BVS, 75 wt% mPDC pre-polymer was mixed with 2.2 wt% Irgacure 819, acting as a primary photoinitiator, and 3.0 wt% Ethyl 4-dimethylamino benzoate (EDAB), acting as a co-photoinitiator, in a solvent of pure ethanol. 3D printing was performed using a homemade micro-continuous liquid production process (MicroCLIP)-based printer. An oxygen-permeable window made of Teflon AF-2400 (Biogeneral Inc., San Diego, CA) was attached to the bottom of the resin vat. A digital micromirror device (DMD, Texas Instruments Inc., Plano, TX) was utilized as the dynamic mask generator to pattern the UV light (365 nm). Projection optics of the printer were optimized to have a pixel resolution of 7.1 μm × 7.1 μm at the focal plane. CAD files of the print part were designed in SolidWorks (Dassault Systèmes, Waltham, MA). The resulting STL files were sliced for a 2D file output by MATLAB (MathWorks Inc., Natick, MA) code developed in-house using a slicing thickness of 5 μm. Full-screen images were projected onto the vat window for photopolymerization. The printed layer thickness was 5 μm, and a printing time of 0.28 s was used for each layer. After printing, the parts were rinsed in ethanol to remove the unpolymerized ink and moved into a heating oven for thermal curing at 120 °C for 12 h.

4.4. Fabrication of DE-BVS

A MediCoat ultrasonic spray coating system (DES1000, Sono-Tek Corporation, Milton, NY) was used for coating the bare BVS with mPOC polymer. To formulate the spray coating ink, 8 wt% mPOC pre-polymer was mixed with 0.55 wt% Irgacure 819 as the photoinitiator and 0, 1, 1.5, 2 and 4 wt% everolimus in the ethanol as solvent. The flow rate of 0.04 mL/min, ultrasonic power of 1.3 W, focusing gas pressure of 1 psi, distance of 5 mm between the nozzle and BVS, the rotation speed of 240 rpm, the horizontal translation speed of 0.1 inch per second, and drying gas pressure of 2 psi were optimized for obtaining a defect-free smooth coating on the surfaces of BVSs. After coating, BVSs were exposed to 365 nm UV light at 330 mW/cm^2 for 2 min to cure the coating layers.

4.5. Scaffold characterization

The structure and surface morphology of the BVSs were observed by scanning electron microscope (SEM; Hitachi S4800, Japan). Strut thickness was measured from cross-sectional SEM images. The radial forces of the BVSs at 50 % compression stain were measured by a radial force tester (RX650, Machine Solutions Inc., AZ). Fourier transformed infrared spectroscopy (FTIR) spectra of BVS coatings with and without drugs were acquired in the attenuated total reflection (ATR) model using a FTIR microscope (LUMOS by Bruker, Billerica, MA).

4.6. Drug release

DE-BVS and BVS (control) were immersed in the media of PBS containing 10 % (v/v) ethanol in order to create an infinite sink condition for released everolimus at 37 °C under 150 rpm agitation [49]. At scheduled time points, i.e. 6, 12, 24, 72 h, 1, 2, 3, 4, 6, 8, 10, 12 weeks, the release media was collected and refreshed. The absorbance of collected media at 278 nm was measured using a microplate reader Cytation 5 (BioTek Instruments, Winooski, VT) according to the pre-determined standard curve.

4.7. Cell culture

Human umbilical vein endothelial cells (HUVECs; ATCC, Manassas, VA) were expanded in growth media consisting of Endothelial Cell Growth Kit-VEGF (ATCC PCS-100-041) in Vascular Cell Basal Medium (ATCC PCS-100-030) under the standard culture condition (37 °C with 5 % CO2 in a humid environment) to 80 % confluency before passaging. HUVECs at passages 5–7 were used. Human aortic smooth muscle cells (HAoSMCs; Cell Applications, Inc., San Diego, CA) were expanded in human SMC growth medium kit (Cell Applications, Inc., 311K-500) under the standard culture condition (37 °C with 5 % CO2 in a humid environment) to 80 % confluency before passaging.

4.8. Cell viability measurement

HUVECs or HAoSMCs were seeded onto 3D-printed substrates without (control) and with the coatings of drug or drug + barrier. After incubation for 24 h, cells were incubated with growth media containing alamarBlue cell viability reagents (Thermo Fisher Scientific, San Jose, CA) for 3 h. After transferring reagents into 96-well plate, the fluorescence of each well was measured at 560/590 nm (excitation/emission) using a microplate reader Cytation 5 (BioTek Instruments). The number of viable cells per well was calculated against a standard curve prepared by plating various concentrations of isolated cells, as determined by the hemocytometer, in triplicate in the culture plates.

4.9. Immunostaining and imaging of cell morphology

Cells on flat and micropillar surfaces were fixed with 4 % formaldehyde (Fisher Scientific, Fair Lawn, NJ) for 10 min and permeated with 0.1 % Triton X-100 for 15 min. Then, the cells were incubated with Alexa Fluor® 594 Phalloidin (10 μM; A12381; ThermoFisher Scientific, Fair Lawn, NJ) and SYTOX™ Green Nucleic Acid Stain (0.15 μM; S7020; ThermoFisher Scientific) in PBS solution with 1.5 % bovine serum albumin for 30 min. The samples were finally washed three times in PBS and mounted on microscope slides for examination using Leica spinning disk confocal microscope.

4.10. Animal model and implantation

Stent implantations were performed at North American Science Associates, LLC (NAMSA) (Minneapolis, MN), accredited by the Association for Assessment and Accreditation of Laboratory Animal Care International. Eight healthy farm swine (castrated male, 3–4 months, weight: 44–54 Kg) underwent device implantation with a targeted balloon-to-artery ratio of 1.0–1.1. Each animal received a single BVS, DE-BVS, or XIENCE DES (3.0 × 8 mm) for 28 days in 3 main coronary arteries, including left anterior descending coronary artery (LAD), left circumflex artery (LCX), and right coronary artery (RCA). RCA of one swine could not be accessed during interventional procedures, and thereby 1 of 8 XIENCE DESs could not be deployed. One of 8 DE-BVS was retrieved following the deployment in LAD of another swine due to scaffold migration. A total of 22 devices (8 BVSs, 7 DE-BVSs and 7 XIENCE DESs) were implanted in 8 swine for 28 days. Intravascular ultrasound (IVUS) was performed before and after the procedure of device implantation and repeated after implantation for 14 and 28 days. 8 swine were euthanized, and hearts were harvested for analysis.

4.11. Histological preparation and staining

Hearts were excised and perfusion fixed with 10 % neutral buffered formalin at 80–100 mm Hg. The implanted coronary arteries were dissected from the heart, radiographed, and dehydrated in a graded series of ethanol solutions. Each artery was trimmed into three pieces, proximal native section, artery sections with the scaffold/stent, and distal native section, with the proximal and distal native sections aiming to be 10 mm away from the ends of the scaffold/stent. All artery sections were embedded in paraffin (all native arteries, 6 arteries with BVS, 5 arteries with DE-BVS) or plastic (all 7 arteries with XIENCE DES, 2 arteries with BVS, 2 arteries with DE-BVS). Then, 2–3 mm sections of arteries with scaffold/stent were cut, and 3 segments from the proximal, middle, and distal portions of each scaffold/stent were sectioned. Paraffin or plastic-embedded tissue sections were cut to 5 μm thickness. One of 7 arteries with XIENCE DES could not be cut into thin tissue sections due to the inappropriate plastic embedding. A total of 8 BVSs, 7 DE-BVSs, and 6 XIENCE DESs were sectioned for histological and immunohistochemistry (IHC) staining. Histomorphometry analysis was performed by staining tissues with hematoxylin and eosin (H&E) and Movat Pentachrome and light microscopic imaging. Inflammation was evaluated by IHC staining of two markers of macrophage – CD 86 and CD163. Vascular tissue recovery was evaluated by IHC staining of alpha-smooth muscle actin (α-SMA) of smooth muscle cells and VE-cadherin of endothelial cells.

4.12. Histomorphometry analysis

Histological sections were measured with computer assisted morphometric analysis by Fiji ImageJ software (https://imagej.net/Fiji), including EEL area (area bound by EEL), IEL area (area bound by IEL), luminal area (area bound by luminal border). After measurements were captured, the following calculations were made, when possible: intimal area (IEL area – luminal area), intimal thickness ({square root (IEL area/pi)} – {square root(luminal area/pi)}), and area stenosis ({1-(luminal area/IEL area)}x100). Inflammation score was calculated by the experienced pathologist based on the following grading parameters.

0 no visible inflammatory response;
1 Individual cells to isolated clusters of cells at the intima/subintima;
2 Individual cells to isolated clusters of cells infiltrating the tunica media;
3 increased numbers of cells/clusters with deeper tunica media infiltration;
4 sheets of cells infiltrating the tunica media with effacement of wall features;

4.13. Statistics and reproducibility

Unless otherwise specified, data was presented as mean ± standard deviation (s.d.). For each experiment, at least three samples were analyzed. One-way ANOVA with Tukey's Multiple Comparison Test was used to analyze statistical significance. A P value of <0.05 was considered to indicate a statistically significant difference. All experiments presented in the manuscript were repeated at least as two independent experiments with replicates to confirm the results are reproducible.

Ethical approval

The animal protocol for our study was approved by the North American Science Associates, LLC (NAMSA) IACUC on December 1, 2022.

CRediT authorship contribution statement

Yonghui Ding: Writing – review & editing, Writing – original draft, Project administration, Methodology, Investigation, Formal analysis, Data curation, Conceptualization. **Liam Warlick:** Methodology, Investigation, Data curation. **Mian Chen:** Methodology, Investigation, Data curation. **Eden Taddese:** Methodology, Investigation, Data curation. **Caralyn Collins:** Methodology, Investigation, Data curation. **Rao Fu:** Methodology, Investigation, Data curation. **Chongwen Duan:** Project administration, Methodology. **Xinlong Wang:** Methodology, Data curation. **Henry Ware:** Methodology, Investigation, Data curation.

Cheng Sun: Writing – review & editing, Writing – original draft, Supervision, Project administration, Methodology, Investigation, Funding acquisition, Formal analysis, Data curation, Conceptualization. **Guillermo Ameer:** Writing – review & editing, Writing – original draft, Supervision, Project administration, Methodology, Investigation, Funding acquisition, Formal analysis, Data curation, Conceptualization.

Declaration of competing interest

The authors declare the following financial interests/personal relationships which may be considered as potential competing interests: Yonghui Ding, Henry Ware, Cheng Sun, and Guillermo Ameer have patent BALLOON DELIVERY SYSTEM FOR DEPLOYMENT OF A SELF-EXPANDING BIORESORBABLE VASCULAR SCAFFOLD pending to Northwestern University. If there are other authors, they declare that they have no known competing financial interests or personal relationships that could have appeared to influence the work reported in this paper.

Acknowledgements

This work was supported by the National Institutes of Health, United States (Grant: R01HL141933). Y. Ding was supported in part by the Center for Advanced Regenerative Engineering and American Heart Association Career Development Award (AHA, Grant: 852772). The authors gratefully acknowledge Connor Alexander Moore and Casey Tan for their technical support in schematic illustration and data analysis, respectively.

Appendix A. Supplementary data

Supplementary data to this article can be found online at https://doi.org/10.1016/j.bioactmat.2024.04.030.

References

[1] S.H. Duda, M. Bosiers, J. Lammer, D. Scheinert, T. Zeller, V. Oliva, A. Tielbeek, J. Anderson, B. Wiesinger, G. Tepe, Drug-eluting and bare nitinol stents for the treatment of atherosclerotic lesions in the superficial femoral artery: long-term results from the SIROCCO trial, J. Endovasc. Ther. 13 (6) (2006) 701–710.
[2] H.M. Burt, W.L. Hunter, Drug-eluting stents: a multidisciplinary success story, Adv. Drug Deliv. Rev. 58 (3) (2006) 350–357.
[3] G.G. Stefanini, D.R. Holmes Jr., Drug-eluting coronary-artery stents, N. Engl. J. Med. 368 (3) (2013) 254–265.
[4] M. Joner, A.V. Finn, A. Farb, E.K. Mont, F.D. Kolodgie, E. Ladich, R. Kutys, K. Skorija, H.K. Gold, R. Virmani, Pathology of drug-eluting stents in humans: delayed healing and late thrombotic risk, J. Am. Coll. Cardiol. 48 (1) (2006) 193–202.
[5] A.V. Finn, G. Nakazawa, M. Joner, F.D. Kolodgie, E.K. Mont, H.K. Gold, R. Virmani, Vascular responses to drug eluting stents: importance of delayed healing, Arterioscler. Thromb. Vasc. Biol. 27 (7) (2007) 1500–1510.
[6] J. Daemen, P. Wenaweser, K. Tsuchida, L. Abrecht, S. Vaina, C. Morger, N. Kukreja, P. Jüni, G. Sianos, G. Hellige, Early and late coronary stent thrombosis of sirolimus-eluting and paclitaxel-eluting stents in routine clinical practice: data from a large two-institutional cohort study, Lancet 369 (9562) (2007) 667–678.
[7] D. Scheinert, S. Scheinert, J. Sax, C. Piorkowski, S. Bräunlich, M. Ulrich, G. Biamino, A. Schmidt, Prevalence and clinical impact of stent fractures after femoropopliteal stenting, J. Am. Coll. Cardiol. 45 (2) (2005) 312–315.
[8] A.J. Klein, S. James Chen, J.C. Messenger, A.R. Hansgen, M.E. Plomondon, J. D. Carroll, I.P. Casserly, Quantitative assessment of the conformational change in the femoropopliteal artery with leg movement, Cathet. Cardiovasc. Interv. 74 (5) (2009) 787–798.
[9] H. Hermawan, D. Dubé, D. Mantovani, Developments in metallic biodegradable stents, Acta Biomater. 6 (5) (2010) 1693–1697.
[10] S. McMahon, N. Bertollo, E.D. O'Cearbhaill, J. Salber, L. Pierucci, P. Duffy, T. Dürig, V. Bi, W. Wang, Bio-resorbable polymer stents: a review of material progress and prospects, Prog. Polym. Sci. 83 (2018) 79–96.
[11] H. Jinnouchi, S. Torii, A. Sakamoto, F.D. Kolodgie, R. Virmani, A.V. Finn, Fully bioresorbable vascular scaffolds: lessons learned and future directions, Nat. Rev. Cardiol. 16 (5) (2019) 286–304.
[12] J.J. Wykrzykowska, R.P. Kraak, S.H. Hofma, R.J. van der Schaaf, E.K. Arkenbout, A.J. Ijsselmuiden, J. Elias, I.M. van Dongen, R.Y. Tijssen, K.T. Koch, Bioresorbable scaffolds versus metallic stents in routine PCI, N. Engl. J. Med. 376 (24) (2017) 2319–2328.
[13] J. Yang, R. Van Lith, K. Baler, R.A. Hoshi, G.A. Ameer, A thermoresponsive biodegradable polymer with intrinsic antioxidant properties, Biomacromolecules 15 (11) (2014) 3942–3952.
[14] D. Bradley, Biomaterial approval opens citrate route to medical implants, Mater. Today 41 (2021) 1.
[15] H. Wang, S. Huddleston, J. Yang, G.A. Ameer, Enabling proregenerative medical devices via citrate-based biomaterials: transitioning from inert to regenerative biomaterials, Adv. Mater. (2023) 2306326.
[16] D. Motlagh, J. Allen, R. Hoshi, J. Yang, K. Lui, G. Ameer, Hemocompatibility evaluation of poly (diol citrate) in vitro for vascular tissue engineering, J. Biomed. Mater. Res. Part A: An Official Journal of The Society for Biomaterials, The Japanese Society for Biomaterials, and The Australian Society for Biomaterials and the Korean Society for Biomaterials 82 (4) (2007) 907–916.
[17] R. Van Lith, E. Baker, H. Ware, J. Yang, A.C. Farsheed, C. Sun, G. Ameer, 3D-Printing strong high-resolution antioxidant bioresorbable vascular stents, Advanced Materials Technologies 1 (9) (2016).
[18] M.Z. Zailani, A.F. Ismail, S.H. Sheikh Abdul Kadir, M.H.D. Othman, P.S. Goh, H. Hasbullah, M.S. Abdullah, B.C. Ng, F. Kamal, Hemocompatibility evaluation of poly (1, 8-octanediol citrate) blend polyethersulfone membranes, J. Biomed. Mater. Res. 105 (5) (2017) 1510–1520.
[19] L. Louis, B.S. Chee, N. Louis, G.G. De Lima, M. McAfee, A. Murphy, M.J. Nugent, Novel polyvinyl-alcohol microsphere for everolimus delivery for subependymal giant cell astrocytoma, J. Drug Deliv. Sci. Technol. 81 (2023) 104204.
[20] S. Torii, H. Jinnouchi, A. Sakamoto, M. Kutyna, A. Cornelissen, S. Kuntz, L. Guo, H. Mori, E. Harari, K.H. Paek, Drug-eluting coronary stents: insights from preclinical and pathology studies, Nat. Rev. Cardiol. (2019) 1–15.
[21] J. Butany, K. Carmichael, S. Leong, M. Collins, Coronary artery stents: identification and evaluation, J. Clin. Pathol. 58 (8) (2005) 795–804.
[22] D.M. Mosser, J.P. Edwards, Exploring the full spectrum of macrophage activation, Nat. Rev. Immunol. 8 (12) (2008) 958–969.
[23] J. Huang, H.O.T. Ware, R. Hai, G. Shao, C. Sun, Conformal geometry and multimaterial additive manufacturing through freeform transformation of building layers, Adv. Mater. 33 (11) (2021) 2005672.
[24] T. Koppara, Q. Cheng, K. Yahagi, H. Mori, O.D. Sanchez, J. Feygin, E. Wittchow, F. D. Kolodgie, R. Virmani, M. Joner, Thrombogenicity and early vascular healing response in metallic biodegradable polymer-based and fully bioabsorbable drug-eluting stents, Circ. Cardiovasc. Interv. 8 (6) (2015) e002427.
[25] K. Kolandaivelu, R. Swaminathan, W.J. Gibson, V.B. Kolachalama, K.-L. Nguyen-Ehrenreich, V.L. Giddings, L. Coleman, G.K. Wong, E.R. Edelman, Stent thrombogenicity early in high-risk interventional settings is driven by stent design and deployment and protected by polymer-drug coatings, Circulation 123 (13) (2011) 1400–1409.
[26] J.A. Ormiston, B. Webber, B. Ubod, O. Darremont, M. Webster, An independent bench comparison of two bioresorbable drug-eluting coronary scaffolds (Absorb and DESolve) with a durable metallic drug-eluting stent (ML8/Xpedition), EuroIntervention: journal of EuroPCR in collaboration with the Working Group on Interventional Cardiology of the European Society of Cardiology 11 (1) (2015) 60–67.
[27] S.J. Lee, H.H. Jo, K.S. Lim, D. Lim, S. Lee, J.H. Lee, W.D. Kim, M.H. Jeong, J.Y. Lim, I.K. Kwon, Heparin coating on 3D printed poly (l-lactic acid) biodegradable cardiovascular stent via mild surface modification approach for coronary artery implantation, Chem. Eng. J. 378 (2019) 122116.
[28] D.-W. Jeong, W. Park, T.M. Bedair, E.Y. Kang, I.H. Kim, D.S. Park, D.S. Sim, Y. J. Hong, W.-G. Koh, M.H. Jeong, Augmented re-endothelialization and anti-inflammation of coronary drug-eluting stent by abluminal coating with magnesium hydroxide, Biomater. Sci. 7 (6) (2019) 2499–2510.
[29] I.T. Meredith, S. Verheye, C.L. Dubois, J. Dens, J. Fajadet, D. Carrié, S. Walsh, K. G. Oldroyd, O. Varenne, S. El-Jack, Primary endpoint results of the EVOLVE trial: a randomized evaluation of a novel bioabsorbable polymer-coated, everolimus-eluting coronary stent, J. Am. Coll. Cardiol. 59 (15) (2012) 1362–1370.
[30] S. Kufner, M. Joner, A. Thannheimer, P. Hoppmann, T. Ibrahim, K. Mayer, S. Cassese, K.-L. Laugwitz, H. Schunkert, A. Kastrati, Ten-year clinical outcomes from a trial of three limus-eluting stents with different polymer coatings in patients with coronary artery disease: results from the ISAR-TEST 4 randomized trial, Circulation 139 (3) (2019) 325–333.
[31] S. Garg, C. Bourantas, P.W. Serruys, New concepts in the design of drug-eluting coronary stents, Nat. Rev. Cardiol. 10 (5) (2013) 248–260.
[32] S.-A. Xie, T. Zhang, J. Wang, F. Zhao, Y.-P. Zhang, W.-J. Yao, S.S. Hur, Y.-T. Yeh, W. Pang, L.-S. Zheng, Matrix stiffness determines the phenotype of vascular smooth muscle cell in vitro and in vivo: role of DNA methyltransferase 1, Biomaterials 155 (2018) 203–216.
[33] Y. Ding, X. Xu, S. Sharma, M. Floren, K. Stenmark, S.J. Bryant, C.P. Neu, W. Tan, Biomimetic soft fibrous hydrogels for contractile and pharmacologically responsive smooth muscle, Acta Biomater. 74 (2018) 121–130.
[34] S. Allahverdian, C. Chaabane, K. Boukais, G.A. Francis, M.-L. Bochaton-Piallat, Smooth muscle cell fate and plasticity in atherosclerosis, Cardiovasc. Res. 114 (4) (2018) 540–550.
[35] G.L. Basatemur, H.F. Jørgensen, M.C. Clarke, M.R. Bennett, Z. Mallat, Vascular smooth muscle cells in atherosclerosis, Nat. Rev. Cardiol. 16 (12) (2019) 727–744.
[36] F. Otsuka, E. Pacheco, L.E. Perkins, J.P. Lane, Q. Wang, M. Kamberi, M. Frie, J. Wang, K. Sakakura, K. Yahagi, Long-term safety of an everolimus-eluting bioresorbable vascular scaffold and the cobalt-chromium XIENCE V stent in a porcine coronary artery model, Circ. Cardiovasc. Interv. 7 (3) (2014) 330–342.
[37] K. Yahagi, Y. Yang, S. Torii, J. Mensah, R.M. White, M. Mathieu, E. Pacheco, M. Nakano, A. Barakat, T. Sharkawi, Comparison of a drug-free early programmed dismantling PDLLA bioresorbable scaffold and a metallic stent in a porcine

coronary artery model at 3-year follow-up, J. Am. Heart Assoc. 6 (6) (2017) e005693.
[38] G.J. Wilson, G. Nakazawa, R.S. Schwartz, B. Huibregtse, B. Poff, T.J. Herbst, D. S. Baim, R. Virmani, Comparison of inflammatory response after implantation of sirolimus-and paclitaxel-eluting stents in porcine coronary arteries, Circulation 120 (2) (2009) 141–149.
[39] D. Ochijewicz, M. Tomaniak, G. Opolski, J. Kochman, Inflammation as a determinant of healing response after coronary stent implantation, Int. J. Cardiovasc. Imag. 37 (2021) 791–801.
[40] B. Lavin, M. Gómez, O.M. Pello, B. Castejon, M.J. Piedras, M. Saura, C. Zaragoza, Nitric oxide prevents aortic neointimal hyperplasia by controlling macrophage polarization, Arterioscler. Thromb. Vasc. Biol. 34 (8) (2014) 1739–1746.
[41] R.A. McDonald, C.A. Halliday, A.M. Miller, L.A. Diver, R.S. Dakin, J. Montgomery, M.W. McBride, S. Kennedy, J.D. McClure, K.E. Robertson, Reducing in-stent restenosis: therapeutic manipulation of miRNA in vascular remodeling and inflammation, J. Am. Coll. Cardiol. 65 (21) (2015) 2314–2327.
[42] X. Ren, Y. Feng, J. Guo, H. Wang, Q. Li, J. Yang, X. Hao, J. Lv, N. Ma, W. Li, Surface modification and endothelialization of biomaterials as potential scaffolds for vascular tissue engineering applications, Chem. Soc. Rev. 44 (15) (2015) 5680–5742.
[43] C. Liang, Y. Hu, H. Wang, D. Xia, Q. Li, J. Zhang, J. Yang, B. Li, H. Li, D. Han, Biomimetic cardiovascular stents for in vivo re-endothelialization, Biomaterials 103 (2016) 170–182.
[44] L.Y. Li, Z. Yang, X.X. Pan, B.X. Feng, R. Yue, B. Yu, Y.F. Zheng, J.Y. Tan, G.Y. Yuan, J. Pei, Incorporating copper to biodegradable magnesium alloy vascular stents via a Cu (II)-Eluting coating for synergistic enhancement in prolonged durability and rapid Re-endothelialization, Adv. Funct. Mater. 32 (47) (2022) 2205634.
[45] P.A. Cahill, E.M. Redmond, Vascular endothelium–gatekeeper of vessel health, Atherosclerosis 248 (2016) 97–109.
[46] K. Zhang, T. Liu, J.A. Li, J.Y. Chen, J. Wang, N. Huang, Surface modification of implanted cardiovascular metal stents: from antithrombosis and antirestenosis to endothelialization, J. Biomed. Mater. Res. Part A: An Official Journal of The Society for Biomaterials, The Japanese Society for Biomaterials, and The Australian Society for Biomaterials and the Korean Society for Biomaterials 102 (2) (2014) 588–609.
[47] R.J. Smith Jr., B. Nasiri, J. Kann, D. Yergeau, J.E. Bard, D.D. Swartz, S. T. Andreadis, Endothelialization of arterial vascular grafts by circulating monocytes, Nat. Commun. 11 (1) (2020) 1622.
[48] Y. Ding, R. Fu, C.P. Collins, S.F. Yoda, C. Sun, G.A. Ameer, 3D-Printed radiopaque bioresorbable stents to improve device visualization, Adv. Healthcare Mater. 11 (23) (2022) 2201955.
[49] C.M. McKittrick, S. McKee, S. Kennedy, K. Oldroyd, M. Wheel, G. Pontrelli, S. Dixon, S. McGinty, C. McCormick, Combining mathematical modelling with in vitro experiments to predict in vivo drug-eluting stent performance, J. Contr. Release 303 (2019) 151–161.